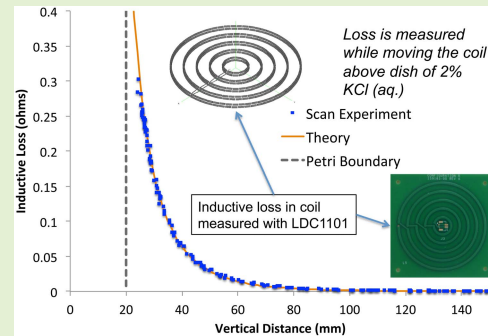# Single-Coil Magnetic Induction Tomography Using the LDC-1101 Chip

Joe R. Feldkamp[ID] and Stephen Quirk

***Abstract*—Single-coil magnetic induction tomography (MIT) has thus far relied upon traditional bridge techniques to measure inductive losses, falling well under ~1 ohm. These measurements have been plagued by both noise and especially drift. This work considers methods based upon the Texas Instruments LDC-1101 chip, which measures LC circuit admittance while in resonance, from which we compute loss. Inductive loss is measured in a 4.0 cm diameter circular loop coil and compared with a quantitative theoretical result while the coil is axially positioned above a 2% aqueous potassium chloride solution contained in a 14 cm diameter petri dish filled to a depth of 2.0 cm. Results accurately capture the tail behavior of inductive loss as a function of coil-target distance. Then, using IR camera technology to track coil position, several 'manual' scans are performed over phantoms prepared from sodium chloride-doped agarose components. In particular, this work considers the ability of single coil scans to capture corners of square plugs, gaps between plugs and side-by-side plugs that differ in conductivity. With drift and noise greatly reduced, the role of sample size is tested, showing that going beyond about 350 samples produces little further benefit to image quality. Though coil position is tracked to within ±0.25 mm, the random nature of manual positioning suggests that a more deliberate positioning scheme is needed, e.g. robotically.**

***Index Terms*— Electrical conductivity distribution, inductive loss, magnetic induction tomography, scanning single coil MIT, Texas Instruments LDC-1101.**

I. INTRODUCTION

MAGNETIC induction tomography (MIT) is a modality intended to image the electrical conductivity distribution of a conductive target [1], [2]. MIT is particularly challenging in medical applications due to low conductivities ($<\sim$1.0 S/m) and correspondingly weak signals. Nevertheless, because electrical conductivity varies naturally between tissue types [3], MIT provides an opportunity to image the features and structures of the body in an alternative manner. In addition, measurable conductivity differences exist between malignant and normal tissues [4] as well as between normal tissue and benign tumors [5], [6]. This natural variation in normal and diseased human tissue suggests that an imaging technique able to accurately capture these intrinsic conductivity differences would provide a medically important diagnostic tool.

MIT is most commonly accomplished using a collection of coils that surround and interact with a conductive target [7], [8]. To improve image resolution, the coil assembly can be translated or rotated relative to the target while sampling inter-coil interactions, which can change substantially as coils approach a target more closely [9], [10]. The quality of image reconstruction is very much dependent upon the number and distribution of samples obtained during a scan, though diminishing image improvement eventually limits additional sampling benefits. For an array of many coils, the number of relative positions and orientations used in order to improve sampling could well be enormous and involve considerable effort to implement. Thus, knowing how much to sample and which coil configurations are optimal can be a challenge [7].

Alternatively, MIT can be accomplished using a single coil that is moved to various locations in the vicinity of a target while collecting coil inductive loss and position data [11]. Coil inductive losses result as the coil's electromagnetic field does work to create eddy currents in the target and can change considerably as a conductive target is approached more closely. As with multi-coil MIT, the quality of an image produced by the reconstruction step depends very much on the distribution and number of samples obtained from a single-coil scan procedure. In previous work, these samples have been acquired

by either using a template [12] that manually guides coil placement prior to collecting a sample, or by tracking coil location during data collection using an IR camera [13], [14]. IR camera tracking, being much faster and accurate, is greatly preferred and allows for a greater number of samples to be acquired in a reasonable time frame. However, without a template to guide positioning, sampling tends to appear essentially random even though positions are known with great accuracy. A third coil-tracking method is through robotic means, or using XYZ sliders to move the coil to numerous programmed locations while collecting a sample at each [15]. Though XYZ sliders are faster and less tedious to implement than the template method, IR camera tracking is still much faster than the three-axis translator approach tested in recent work [14], [15].

Regardless of scanning methods used to date, the accurate acquisition of a large number of inductive loss samples has been hampered by the drift that occurs in instrumentation during a scan, which can last as long as 15 minutes when using either the template or XYZ translator methods. In addition to drift, prior instrumentation has been plagued by noise. Without a reduction in both noise and drift, current instrumentation has not been sufficiently adequate to explore the role of sampling number and distribution.

This has been recently addressed with newer instrumentation based upon the Texas Instruments (TI) LDC-1101 'inductance-to-digital' converter. TI offers a family of chips similar to the LDC-1101, each of which delivers particular advantages. The LDC-1101 was chosen because of its frequency range, resolution and convenient SPI interface to commercial micro-controllers. In addition to its ability to measure the impedance of an LC tank circuit at resonance, the LDC-1101 also allows measurement of resonant frequency when using an external time base – a feature needed for loss measurement. Unlike earlier generations of instrumentation, which kept frequency fixed while inductive loss was measured, the oscillation frequency of the LC tank circuit coupled to the LDC-1101 varies slightly during a scan due to stray capacitance effects. Thus, frequency should usually be measured and included in image reconstruction. Further background is given in a later section II-A.

Given that newer instrumentation based upon the LDC-1101 is able to reduce drift and noise compared with older instrumentation, as this work shows, the quality of single-coil MIT results can be evaluated when the number of available samples becomes essentially unlimited. A key question to answer here is whether or not this enlarged data set can be acquired using a more or less random scan, even though acquired with great accuracy, or whether a more methodical scan is necessary. Furthermore, with an ability to collect an unlimited amount of data, this work intends to determine when the point of diminishing returns has been reached where additional sampling yields no further benefit to image reconstruction. A much more methodical scan could be ensured by acquiring samples over a regular lattice or a lattice generated strategically – as by a Latin Hypercube assignment of positions [16]. Lattice type methods would likely require a robotic positioning system to place the sensor coil at some set of predetermined locations and possibly include IR tracking to help facilitate speed. Here, random sampling via IR tracking is rigorously tested by carefully evaluating a set of agarose gel lab phantoms that provide a range of resolution challenges.

Phantoms chosen here consist of square, higher conductivity inclusions embedded in lower conductivity agarose gel background. Various sub-features are included that test the resolving ability of MIT. These features consist of the sides and corners of individual square plugs, plug spacing and the relative orientation of multiple squares. In some cases, squares have unequal conductivity. Corners are expected to be challenging given that a corner does not readily accommodate the inherently circular pathway of an eddy current. On the other hand, eddy currents will not likely be hindered or corrupted by inclusions consisting of straight, or nearly straight sides. Thus, corner resolution can only be expected to the extent that eddy current loops can 'fit' into or pass through a corner.

In spite of sampling strategies, phantom corners may be unresolvable and lead to circular images. Thus, square inclusions are stretched to determine whether the long axis eventually becomes distinct from the short axis. Correct resolution of a rectangular inclusion's length and width is assessed as its aspect ratio is increased. Also considered are staggered square inclusions situated along the diagonal of a square-shaped phantom while separation distance between inclusions is varied. Scans are made of phantoms with the intention of determining how close inclusions can be to each other and still recognize the presence of a gap.

Finally, two inclusions differing in conductivity are considered in an effort to see whether side by side features can be recognized as distinct when their conductivity is different. So there is an entire hierarchy of features at different scales likely present in real specimens, which may require resolution. Performance may need to be explored for different coil sizes to ensure optimal coil selection [17]. Furthermore, consideration of various phantom features or sub-features can help understand whether random sampling is able to correctly capture structure when sampling is increased. A goal of this work is to know more clearly whether lattice-like positioning of the coil is needed or if the inevitable random and arbitrary sampling associated with the IR tracking camera is acceptable.

II. INDUCTIVE LOSS – THEORY VS. EXPERIMENT

In order to create an image of electrical conductivity within a target from simultaneous inductive loss and corresponding coil position measurements, a mapping is needed between the electrical conductivity distribution and the inductive losses measured in a coil during the course of a scan. Inductive loss is simply a manifestation of the work required by a coil's alternating field in order to drive eddy currents, which for targets of biological interest is no more than a few tenths of an ohm. Since the loss is so small, the effects of noise and drift can be considerable. This was previously dealt with by keeping scan time sufficiently short to limit drift and through specialized denoising schemes [18]. The next few subsections provide background on an alternative measurement strategy involving TI's LDC-1101 'inductance-to-digital' converter and how its results compare with theory.
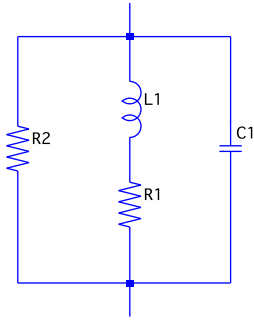
Fig. 1. An equivalent circuit commonly used to represent real inductors, consists of ideal inductance L_1, ideal capacitance C_1 and ideal resistances R_1 and R_2.

A. Inductive Loss From the LDC-1101

A real inductor, here a set of concentric circular loops on a PCB, can be conveniently represented as a simple equivalent circuit, which can also be related to theoretical results. Referring to Figure 1, resistance R_2 is ordinarily regarded as infinite and is absent in a similar circuit shown in the LDC-1101 datasheet published by TI [19]. *Click here for product info.* In applications, TI's chip measures the admittance $\bar{Y}$ of the circuit shown in Figure 1 when in resonance.

$$\bar{Y} = \frac{1}{R_2} + \frac{R_1}{R_1^2 + \omega^2 L_1^2} \qquad (1)$$

If $\bar{Y}$ is measured with sufficient accuracy, then the loss associated with inductor L_1, i.e. R_1, may be measured. There are two sources of inductive loss, one associated with the metallic winding of the coil, R_l, which may be impacted by temperature; and, also the loss of interest here – that due to eddy currents generated within the weakly conductive target, R_e. Both of these are expected to be very small compared with the inductive reactance, so we have, by approximation:

$$\bar{Y} \cong \frac{1}{R_2} + \frac{R_1}{\omega^2 L_1^2} \; ; \quad R_1 = R_l + R_e \qquad (2)$$

Two measurements are needed to obtain the inductive loss related to just eddy currents: one while the coil is far removed from any conductive object; and a second while the coil is near the target. For typical scans over a target, including both far and near measurements, oscillation frequency changes very little. In a representative scan over an agarose phantom with conductivity ~ 1.0 S/m, LDC1101 oscillation frequency is 8.6349 MHz while the standard deviation across nearly 2000 samples is 0.00633 MHz and the maximum variation is 0.02442 MHz. So considering R_2 as infinite, subtracting $\bar{Y}\omega^2$, obtained when the coil-target distance is large, from any other measurements yields the loss due to eddy currents:

$$R_e = \left(\bar{Y}\omega^2 - \bar{Y}_\infty \omega_\infty^2 \right) L_1^2 \qquad (3)$$

Equation (3) is the formula used in practice to determine inductive loss during the course of a scan. Free space admittance is measured twice – once at the beginning of a scan, and also at the end of a scan to compensate for baseline drift. Admittance is presumed to drift linearly with time during the course of a scan and a subtraction is performed as indicated in (3) using a baseline corrected $\bar{Y}_\infty$.

In our circuit, R_2 is set to 20 kΩ in order to yield better performance, achieving lower noise and more stable oscillation within the LDC1101. The error ε committed by considering R_2 as infinite is:

$$\varepsilon = \left(\omega_\infty^2 - \omega^2 \right) L_1^2 / R_2 \qquad (4)$$

During a typical scan using the LDC1101, frequency may vary by as much as 0.025 MHz with RMS variation of 0.00633 MHz while oscillation frequency in the LDC1101 is 8.835 MHz (measured using a 16.00 MHz clock as time base). Corresponding error from (4) is at most 0.00384 Ω while the RMS error is ~ 0.001 Ω. By contrast, error associated with the approximation inherent in (2) is at most ~ 0.001 Ω since inductive reactance for the coils we use is ~ 120 Ω while eddy current losses in our coils are nominally ~ 0.1 Ω. These loss errors have ramifications when using inductive loss and corresponding coil position data to perform image reconstruction.

Furthermore, the circuit of Figure 1 is itself an approximation since the capacitance C_1 may have losses associated with it; i.e., not ideal as originally proposed. C_1 is actually comprised of additional capacitances: that due to the coil and those due to the circuit that the coil connects to either inside the LDC-1101 or external capacitances used to tune the circuit to a suitable frequency (TI specifies an upper limit of 10 MHz for this chip). Either of these capacitances can display unwanted losses, which can spoil the accuracy of measuring R_e, a topic of the next section – note that only an inductive loss originating from eddy currents is sought in our MIT application. Other applications for the LDC-1101 may not require exclusion of capacitive losses. LDC1101 based electronics is shown in the Appendix.

B. Comparison With Theory

The inductive loss due to eddy currents, as represented by (3) can be compared to an available theoretical prediction, providing an accuracy check of the LDC-1101 inductance-to-digital converter. As specified by the LDC-1101 data-sheet, this device is capable of measuring LC circuit impedance with 16-bit precision, at least as we have configured the chip. However, this does not answer the question of accuracy. In previous work, a mathematical model was developed for computing inductive losses in concentric circular loop coils which has no adjustable parameters. The model assumes an isotropic medium, uniform permittivity and magnetic permeability, but otherwise allows electrical conductivity to vary arbitrarily in all three dimensions. Due to a perturbative expansion technique applied to Maxwell's equations, electrical conductivity of the target is limited to be less than ~ 200 S/m, which is an acceptable restriction for many materials of interest, including a wide variety of biological [4] and geological specimens [20].

As shown in previous work, inductive loss in concentric circular loop coils, which may be layered if the distance between layers is negligible compared to loop diameter, is given as a convolution on electrical conductivity over the

TABLE I
SYMBOLS APPEARING IN KERNEL AND LOSS FORMULA

| Symbol	Quantity	Units & Common Abbreviations
$\sigma(\vec{r})$	electrical conductivity	Siemens/m, or (S/m)
ρ_k	radial distance from coil axis to loop k	centimeters, or cm
ρ	radial distance from coil axis to field point	centimeters, or cm
z_c	perpendicular distance from coil plane to field point	centimeters, or cm
μ	magnetic permeability	$4\pi \times 10^{-7}$ H/m
ω	field angular frequency	π radians/second

Fig. 2. Comparison of inductive loss measurements using the LDC-1101 with results computed from (5). Measurements were taken over a 14 cm diameter petri dish filled to a depth of 2.0 cm – dashed line represents the 2.0% KCl (aq) surface.

target volume [21]. In this work, we used a two-layer coil printed on a PCB, with each layer consisting of 5 concentric loops of radii 0.4, 0.8, 1.2, 1.6 and 2.0 cm – pictures and more details are given in [17]. Letting the vector $\vec{c}$ locate the coil center relative to the lab coordinate system (CS) origin, and the vector $\vec{r}$ locate the field point, also in the lab CS, and with $\tilde{R}$ a transformation from coil frame to lab frame coordinates, we have:

$$\delta Z(\vec{c}) = \int \sigma_l(\vec{r}) \, G\left(\tilde{R}^T(\vec{r} - \vec{c})\right) dx\,dy\,dz \qquad (5)$$

The 'coil CS' origin is located at the coil center, with Z-axis perpendicular to the coil plane. Conductivity is subscripted as a reminder that electrical conductivity is computed from the point of view of the lab frame, rather than the reference frame centered on the coil. The 'kernel' of the convolution integral is given as a sum over the circular, concentric loops:

$$G(\vec{r}_c) = \frac{\mu^2 \omega^2}{4\rho\pi^2} \sum_{j,k} \sqrt{\rho_j \rho_k} \, Q_{1/2}(\eta_j) \, Q_{1/2}(\eta_k) \qquad (6)$$

Arguments for the circularly symmetric toroid (or ring) function $Q_{1/2}$ (see Appendix) lie in the interval $1 < \eta < \infty$ and are related to field position by [23]:

$$\eta_j = \frac{\rho^2 + \rho_j^2 + z_c^2}{2\rho\rho_j} \qquad (7)$$

For practical calculations, the convolution integral is numerically computed using a finite element mesh over the target specimen. We use linear deformed prismatic elements and 9-point integration over each element [24]. The analytical, closed-form formula has been rigorously tested in previous work [11], [14], [22] and shown to be quantitative in measurements over tanks of aqueous potassium chloride (KCl) with carefully measured dimensions. Previous electronics measured inductive loss using standard bridge techniques, as described in [11].

Here, we view (5) as exact and want to verify the accuracy of the LDC-1101. The target specimen consisted of a 14.0 cm diameter petri dish, filled to a depth of 2.0 cm with 2.0% KCl(aq). Using the IR camera for tracking the coil center [13], [14], the coil-enclosure was moved vertically along the petri dish axis, ranging from just a few mm above the liquid surface to a distance of about 130 mm above the liquid surface. As noted in previous work, coil location can be tracked to within about ± 0.25 mm [14], [29]. Though manual
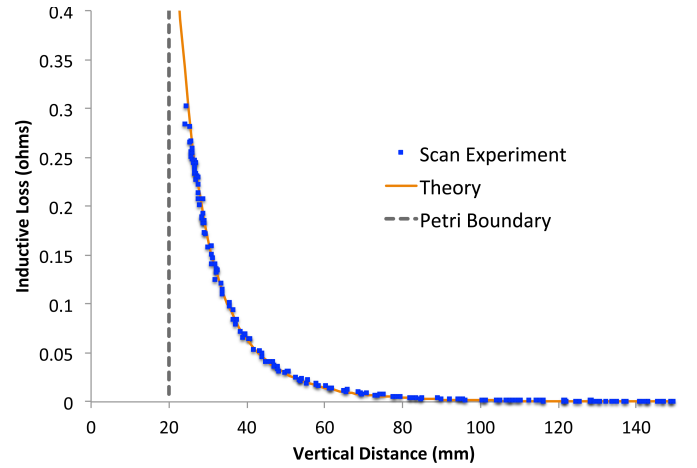
positioning along the axis is by no means perfect, we assumed that it was perfect for the purpose of theoretical calculations. While scanning, the coil was kept parallel to the KCl(aq) surface to the extent possible, and considered perfectly parallel in calculations. Figure 2 gives a comparison between experimental and theoretical results.

The result shown in Figure 2 is quite good, indicating that instrumentation based on the LDC-1101 faithfully captures the 'tail' of the decaying signal. Especially noteworthy is that there are no fitting parameters that are adjusted to improve agreement. Rather, both theoretical and experimental data points are compared without further processing. The small amount of discrepancy between theory and experiment is due to an inability to manually move the coil perfectly along the petri dish axis, without deviation. Though accuracy is excellent in this comparison, performance of the LDC-1101 under different conditions has not been verified – such as lower frequency. We note here that TI application documentation indicates a number of constraints to ensure best performance, such as amount of parallel capacitance used, inductance, oscillation frequency and setup specific to the LDC-1101.

Figure 3 provides an indication of the amount of noise and drift typically experienced while measuring loss over a 100 second time period. Various saline-based targets are placed near the coil to briefly measure inductive loss – salt levels were deliberately tuned to yield coil responses from ∼0.1 to ∼0.5 Ω, covering the most common range for biological applications. A variety of similar tests indicate that raw data show a RMS noise level of ± 0.00043 Ω. Using stationary wavelets [25] to denoise the signal reduces the noise level to ± 0.00012 Ω. Given the encouraging results of Figures 2 and 3, a sequence of agarose phantoms, presenting a range of challenges, is scanned and subjected to image reconstruction.

III. IMAGING 2D PHANTOMS WITH THE LDC1101

Loss measurements based upon the LDC-1101 have proven to be less noisy and exhibit much less drift than our
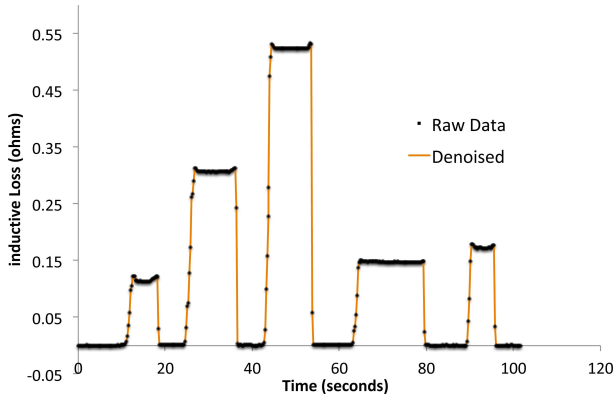
Fig. 3. Illustrates level of noise and drift while data are collected by positioning the coil near various saline-based targets. Salt level is adjusted to yield responses in the ~0.1 to ~0.5 Ω range.

Fig. 4. Phantom 1 – plugs spaced 5.0 mm, corner-to-corner.

previous instrumentation. Remaining drift is nearly linear and can be subtracted out with little effort by measuring free space admittance both before and immediately after a scan, providing an effective background baseline. Improved performance has enabled reliable collection of larger datasets that are essentially immune to noise and drift, at least compared to older instrumentation. The steps used to build electrical conductivity images consist of: 1) manual scan of phantoms which includes capturing coil inductive losses together with corresponding coil locations using an IR camera; 2) denoising inductive loss data using a known stationary wavelet transform procedure [25]; and, 3) two-dimensional image reconstruction based upon regularized, constrained optimization [21]. Three dimensional imaging was not used since phantoms used here are 2-dimensional.

A. 2D Image Reconstruction

After discretizing convolution integral (5) using deformed prismatic finite elements (1,464 elements, 783 nodes), a system of equations is produced that predicts coil loss, $\tilde{A}\vec{\sigma}$, at each coil position, while $\delta\tilde{Z}_m$ is the actual set of measurements. A non-negative least squares problem is set up and regularized via diagonal penalty matrix $\tilde{D}$:

$$\min \quad \frac{1}{2}\left\|\tilde{A}\vec{\sigma} - \delta\tilde{Z}_m\right\|_2^2 + \frac{1}{2}\tau^2\left\|\tilde{D}\left(\vec{\sigma} - \vec{\sigma}_{avg}\right)\right\|_2^2$$
$$s.t. \quad \vec{\sigma} \geq 0 \tag{8}$$

After converting (8) to standard form [26], as shown in [21], image reconstruction proceeds via singular value decomposition (SVD) of the matrix $\tilde{A}\tilde{D}^{-1}$. Solution non-negativity is enforced through application of KKT (Karush-Kuhn-Tucker) multipliers and active set technology. The global regularization parameter is found by stepping τ through the singular values produced by the SVD, from largest to smallest. The process is stopped when the solution error norm approaches the inductive loss vector error norm from above – known as the discrepancy principle [27]. A 'placebo' scan was completed over the Styrofoam stage in the absence of a phantom. The background noise level for this 'placebo' was found to be ± 0.001 Ω, which is similar to the error referred to immediately after
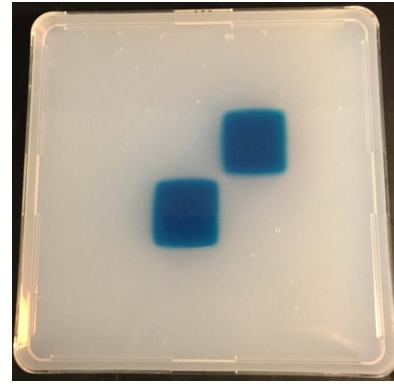
Equation (4) of section II. To comfortably avoid the noise floor of the instrument, our stopping condition here was set 10× higher, at 0.01 Ω.

Up to five iterations may be needed for each singular value tested in order to satisfy KKT conditions. Though the penalty matrix can be set up to weight solutions at each node differently, $\tilde{D}$ was set to the identity matrix in this work. Solution of minimization problem (8) is discussed at length in a recent publication [21], and not covered here in detail. In general, if the stopping condition is reached while τ is yet large, the image is usually over smoothed due to an excessive penalty term. To facilitate image comparison, an identical two-color scheme is used throughout – light blue to dark blue at mid-scale; dark red at mid-scale to yellow; black is exactly at the mid-scale point. This provides a crisp distinction between higher and lower conductivity regions in the image, aiding feature recognition.

B. Agarose Phantom Designs

A sequence of 2D phantoms was prepared, each consisting of sodium chloride (NaCl) doped square plugs of agarose embedded in a background of un-doped agarose, which has a conductivity ~0.2 S/m. Plugs are 5 cm square and embedded in agarose-filled, 23 cm square petri dishes, ~2 cm deep. Un-doped agarose was prepared at 1.8% w/v using distilled, deionized water. Agarose plugs were doped with either 0.006 g/mL NaCl or 0.012 g/mL NaCl. Space for the plugs was cut out using a 'cookie cutter' and then backfilled with melted, NaCl-doped agarose. Though not measured here, measurements taken in other work indicate that corresponding conductivities are about 1.0 S/m and 2.0 S/m respectively, which is consistent with literature agarose values [28]. All phantoms were covered with a sheet of thin plastic film wrap to prevent direct coil contact with the moist phantom surface while scanning.

Two plugs were diagonally arranged along the petri dish diagonal, with either a space of ~5mm between corners or with no gap at all. These two phantoms are shown in Figures 4 and 5. The next pair of phantoms simply moves the upper right plug lower so that it overlaps just 50% of the lower left plug along their common boundary. The first in this set continues to keep the level of NaCl doping the same for
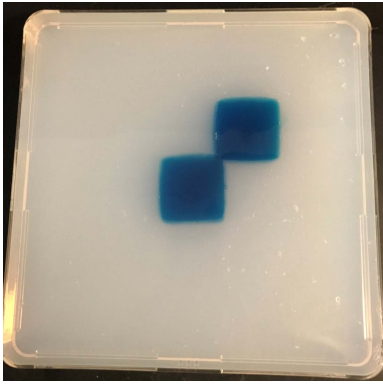
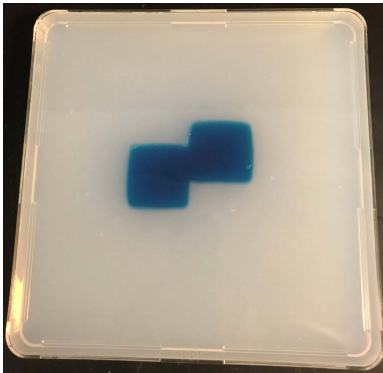Fig. 5.   Phantom 2 – plugs touch at their corners.

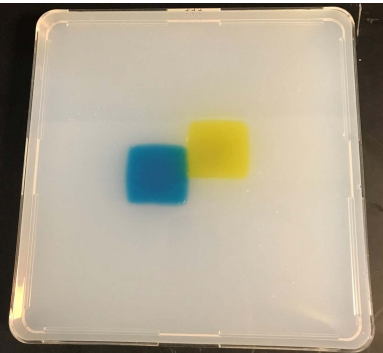Fig. 6.   Phantom 3 – plugs overlap 50% along their touching sides.

Fig. 7.   Phantom 4 – plugs overlap 50% along their touching sides; blue plug has half the conductivity of the yellow one.
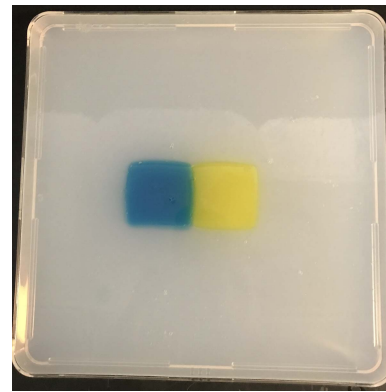

Fig. 8.   Phantom 5 – plugs are side-by-side; blue plug has half the conductivity of the yellow one. Phantom 6, not shown, dopes both plugs at the higher level of 0.012 g/mL NaCl.

each plug, at 0.006 g/mL of agarose gel, while the second doubles NaCl doping in the plug situated to the upper right. Photos for these two phantoms are shown in Figures 6 and 7.

The final contrasting pair of phantoms places the two plugs exactly side by side, as indicated in the photo of Figure 8, either with the right side plug given twice the level of NaCl doping (shown), or with identical doping for each at the higher level of 0.012 g/ml (not shown).

C. Image Reconstruction Results for Agarose Phantoms

As discussed in section III-A, assignment of the 'global' regularization parameter τ, consistent with the stopping condition, ultimately determines the quality of a reconstructed image

for each of our phantoms. So this is always made as small as possible without violating the stop criterion formalized by the discrepancy principle [27]. Generally, if a larger τ value is assigned because the stopping condition has already been reached, then images appear smoother and predicted conductivity values will be less accurate.

A related issue that impacts solution accuracy is the requirement that dielectric constant must be fixed throughout all space. Though dielectric constant does not appreciably change between agarose plugs and background, there is a substantial change at the borders of the square petri dish where agarose and plastic-air meet, from ∼75.0 down to ∼1.0 [17]. From validation work reported in [22], the presence of a significant decrease in dielectric constant will produce an exaggerated prediction of electrical conductivity. When viewing any of our image reconstructions here, it is noted that along all of the petri boundaries, predicted conductivity is higher than the expected value of ∼0.2 S/m. Because of the lateral reach of the field [12], avoiding a 'boundary effect' on image reconstruction would require keeping the coil center several coil diameters away from the petri boundary during a scan, which is not practical with the phantoms used in this work. Alternatively, boundary effects can be completely avoided by using a circular petri dish and sampling entirely along the petri axis – also not practical for heterogeneous phantoms. Note that the data of Figure 2 were acquired in precisely this manner.

The MIT images associated with phantoms 1 and 2 are shown in Figures 9 and 10, using the 2-scale coloration scheme with a black line segregating the two ranges from each other. This particular color scheme provides the best opportunity to distinguish or delineate regions with the greatest clarity. The reconstructed images show clear separation of the two plugs when they aren't touching. However, when touching with small overlap, the reconstructed image of the plugs shows them with more of a bridge between them than there really is according to Figure 5. Each plug is correctly showing nearly the same conductivity, as they should, inasmuch as they are equally doped with NaCl.

In either case, the scan consists of ∼1000 loss and corresponding position samples. Yet, the rank of the model matrix
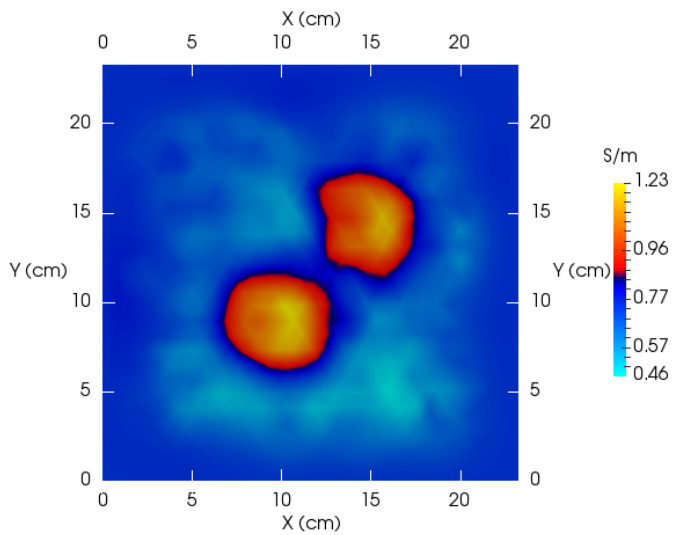
Fig. 9.   Phantom 1 – reconstructed image associated with the phantom shown in Figure 4.
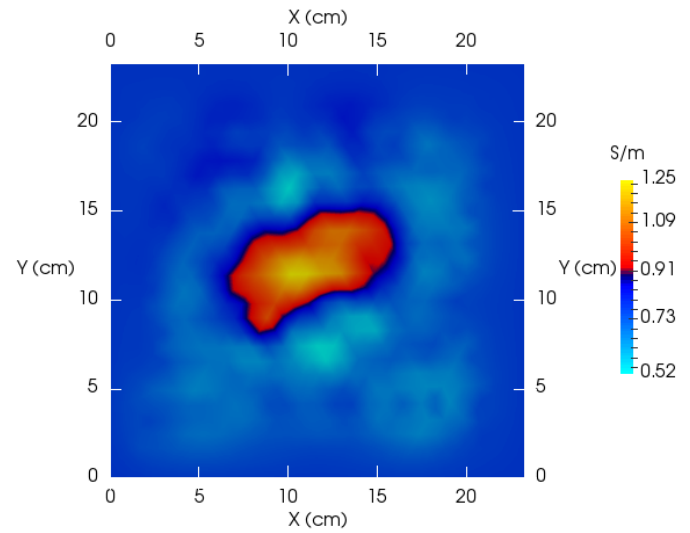

Fig. 11.   Phantom 3 – reconstructed image associated with the phantom shown in Figure 6.
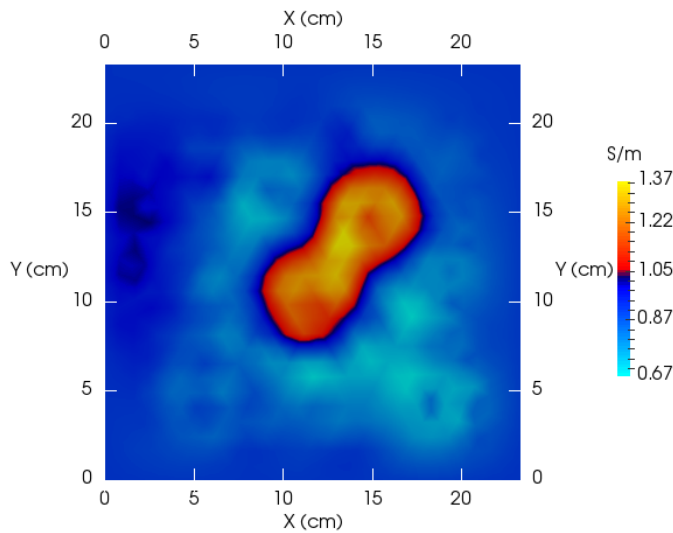

Fig. 10.   Phantom 2 – reconstructed image associated with the phantom shown in Figure 5.
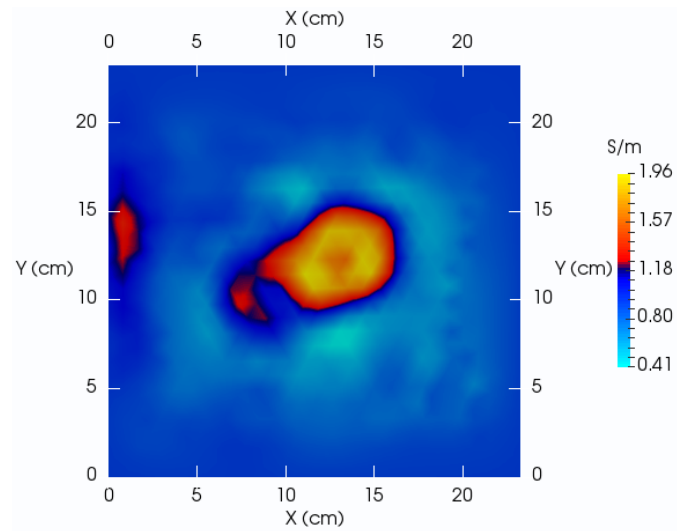

Fig. 12.   Phantom 4 – reconstructed image associated with the phantom shown in Figure 7.

$\tilde{A}$ is far less, about 360, indicating that the large number of samples acquired here has produced no additional benefit. This was verified by doing a scan with 2000 samples, though yielding no significant image improvement. To improve rank, and thus image quality, samples would need to be chosen in a more methodical manner rather than manually. Overall, phantoms that produce larger signal variability, usually due to the presence of higher conductivity features, generally produce more accurate conductivity values since we are then more likely in a position to assign a smaller global regularization value without violating the discrepancy principle.

Figures 11 and 12 show the reconstructed images for phantoms (3 and 4) built with plugs overlapping along their boundaries, corresponding to Figures 6 and 7. The only difference between these two phantoms and their reconstructions

is the $2\times$ larger conductivity value for the upper right plug. In either case, the positions and sizes of the plugs match the physical phantom, while images correctly indicate the expected conductivity change from lower left to upper right plugs – uniform for Figure 11 (phantom 3), but nearly $2\times$ increase in Figure 12 (phantom 4). As noted, all phantoms display a conductivity exceeding expectations along the petri border, which is due to the strong contrast in relative permittivity there. The effect is especially noteworthy for phantom 4 along the phantom left border, which in this case was deliberately scanned to sample more points along the phantom's left border. The actual sampling locations for this replicate of phantom 4 are shown in Figure 13 to illustrate the extra emphasis that was given at the phantom's left hand side just to enhance the effect of a relative permittivity constrast – from ~75.0 down to ~1.0.
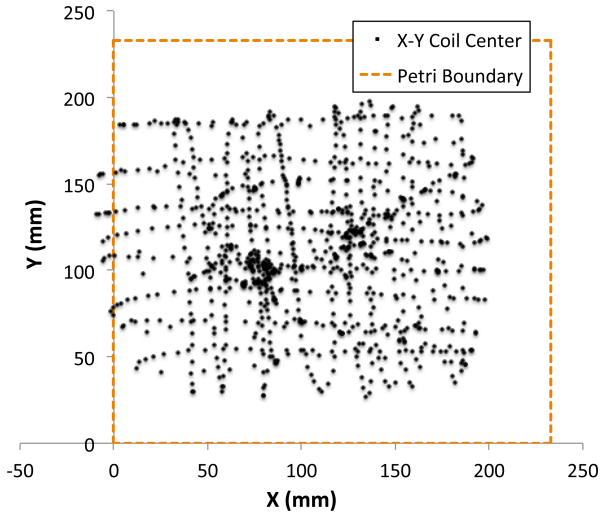
Fig. 13. Shows locations visited by coil (origin) during course of scanning Phantom 4 with IR camera tracking ~1000 locations – see Figure 12.
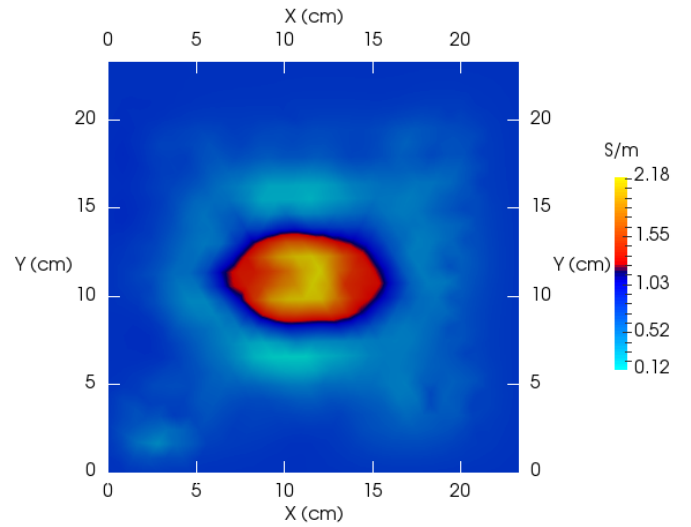

Fig. 15. Phantom 6 – reconstructed image associated with the phantom shown in Figure 8, except that both plugs are doped at the higher NaCl level.
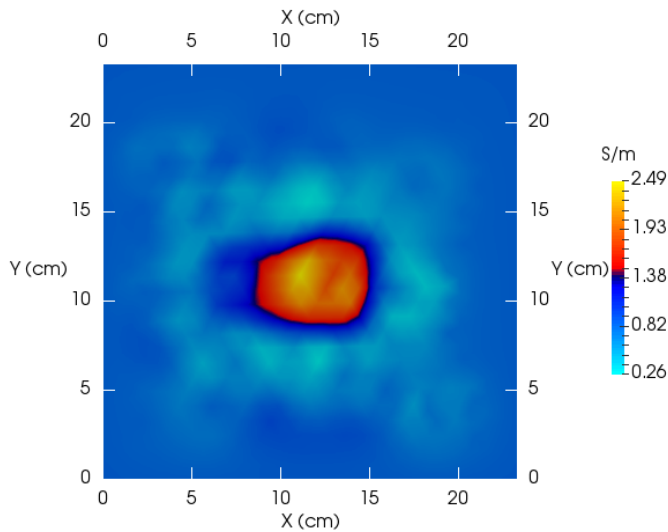

Fig. 14. Phantom 5 – reconstructed image associated with the phantom shown in Figure 8.

Figures 14 and 15 show the reconstructed images for our remaining two phantoms, each with side-by-side square plugs. In the first figure, the right hand plug has $2\times$ the conductivity of the left hand plug. The presence of each plug is indicated, each showing the appropriate conductivity, shape and location. For the last phantom, the two side-by-side plugs present the correct conductivity and locations. However, shape of the two plugs together is more oval than rectangular. Generally, none of the reconstructed images correctly capture the corners of the square plugs. Instead, they appear essentially rounded for most of the phantoms. Exceptions could be found in Figure 14 and possibly Figure 11. This could possibly be improved by using a more lattice-like scan that contributes to a higher rank model matrix, which in turn permits a greater reduction in global regularization τ. Also, a smaller diameter coil might be preferable [17], perhaps allowing for greater development of eddy currents into plug corners.

IV. CONCLUSION

Single coil scanning MIT experiments have shown that the LDC-1101 chip from TI is an effective device for measuring coil loss, not only functioning with negligible drift and noise compared to earlier bridge methods, but also with excellent accuracy, especially as noted in Figure 2. Because of reduced drift and noise issues, we have been able to examine the extent to which increased sampling during MIT scans produces benefits for image reconstruction. Using the IR camera to track coil position to within ± 0.25 mm, hand scanning led to no discernible benefit when acquiring beyond ~360 samples, essentially due to the randomness naturally produced by hand scanning. This agrees with the rank determined for our 'impedance' matrix, which is typically ~360. It was also confirmed by performing scans that sampled 400, 1000 and 2000 positions without seeing a benefit.

In general, the dominant corner features of the plugs used to build phantoms where difficult, if not possible to resolve. This may be due, in part, to the particular coil that we used, inasmuch as previous work [17] showed that smaller diameter coils may improve image fidelity. For example, using an excessively large diameter coil may discourage the formation of eddy currents within corners. However, smaller coils will likely have limited depth perception and not reveal features at greater depth. Perhaps of greatest importance is an inability to leverage larger data sets when samples are manually acquired. With such sets, the probability of acquiring redundant samples only increases as sample size grows. In fact, this is clearly indicated in Figure 13 which provides the sampling locations associated with the scan of phantom 4 (Figures 7 and 12).

Clearly, there is a need to increase sampling during scans, but only if done in a manner that is truly effective, as would be determined by the rank of our model matrix $\tilde{A}$ – a rank of ~ 360 was the best that either of the authors could achieve in hand scans. A better method would very likely involve a robotic scan that allows us to 'program in' a preferred lattice of samples to acquire, likely that provided by the Latin hypercube sample. For that, plans are in place to repurpose a 3D printer
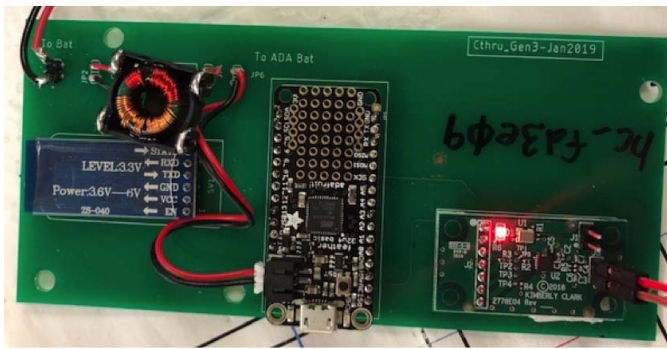
Fig. 16. Motherboard consisting of three smaller boards – custom LDC1101 board is at far right, Feather 32u4 microcontroller middle, HC-05 Bluetooth module at far left.

to allow for single-coil MIT scans to be accomplished that pay attention to sampling location. Scans would likely again track coil position with our IR camera so that acquisition can proceed nonstop. For such scans to work, we reiterate that maintaining a low-drift and low-noise condition throughout the scan are imperative. And for that, the LDC-1101 seems to be very well-suited.

APPENDIX

Ring Function: A suitable definition for the ring function, first presented in section (2), is given as an integral formula by Gradshteyn and Ryzhik [23] on page 1001:

$$Q_{1/2}(\eta) = \frac{1}{\sqrt{2}} \int_0^{\pi} \frac{\cos(t)dt}{\sqrt{\eta - \cos(t)}} \tag{9}$$

Rather than work from Equation (9), a hypergeometric form of Equation (9) was found to be much more efficient for computational work and is found on page 1022 of the same reference.

Electronics: Figure 16 reveals the overall simplicity of the LDC1101 based instrumentation for measuring inductive loss and LC tank circuit resonant frequency. The smaller board at the right hand side of the motherboard was custom built, while the remaining two boards are commercially available.

REFERENCES

[1] H. Y. Wei and M. Soleimani, "Electromagnetic tomography for medical and industrial applications: Challenges and opportunities," *Proc. IEEE*, vol. 101, no. 3, pp. 559–564, Mar. 2013.

[2] H.-Y. Wei and M. Soleimani, "Three-dimensional magnetic induction tomography imaging using a matrix free Krylov subspace inversion algorithm," *Prog. Electromagn. Res.*, vol. 122, pp. 29–45, Jan. 2012.

[3] S. Gabriel, R. W. Lau, and C. Gabriel, "The dielectric properties of biological tissues: II. Measurements in the frequency range 10 Hz to 20 GHz," *Phys. Med. Biol.*, vol. 41, no. 11, pp. 2251–2269, Nov. 1996.

[4] W. T. Joines, Y. Zhang, C. Li, and R. L. Jirtle, "The measured electrical properties of normal and malignant human tissues from 50 to 900 MHz," *Med. Phys.*, vol. 21, no. 4, pp. 547–550, Apr. 1994.

[5] H. Wang *et al.*, "Dielectric properties of human liver from 10 Hz to 100 MHz: Normal liver, hepatocellular carcinoma, hepatic fibrosis and liver hemangioma," *Bio-Med. Mater. Eng.*, vol. 24, no. 6, pp. 2725–2732, 2014.

[6] R. DeLonzor, R. K. Spero, and J. J. Williams, "The electrical conductivity of *in vivo* human uterine fibroids," *Int. J. Hyperthermia*, vol. 27, no. 3, pp. 255–265, May 2011.

[7] H. Scharfetter, K. Hollaus, J. Rosell-Ferrer, and R. Merwa, "Single-step 3-D image reconstruction in magnetic induction tomography: Theoretical limits of spatial resolution and contrast to noise ratio," *Ann. Biomed. Eng.*, vol. 34, no. 11, pp. 1786–1798, Nov. 2006.

[8] H. Scharfetter, P. Brunner, and R. Merwa, "Magnetic induction tomography: Single-step solution of the 3-D inverse problem for differential image reconstruction," *Int. J. Inf. Syst. Sci.*, vol. 2, no. 4, pp. 585–606, 2006.

[9] B. Dekdouk, C. Ktistis, D. W. Armitage, and A. J. Peyton, "Absolute imaging of low conductivity material distributions using nonlinear reconstruction methods in magnetic induction tomography," *Prog. Electromagn. Res.*, vol. 155, pp. 1–18, Jan. 2016.

[10] K. Stawicki and S. Gratkowski, "Optimization of signal coils in the magnetic induction tomography system," *Przegląd Elektrotechniczny*, vol. 86, no. 5, pp. 74–77, 2010.

[11] J. R. Feldkamp, "Single-coil magnetic induction tomographic three-dimensional imaging," *J. Med. Imag.*, vol. 2, no. 1, Mar. 2015, Art. no. 013502.

[12] J. R. Feldkamp and S. Quirk, "Effects of tissue heterogeneity on single-coil, scanning MIT imaging," *Proc. SPIE*, vol. 9783, Mar. 2016, Art. no. 978359.

[13] J. R. Feldkamp and S. Quirk, "Optically tracked, single-coil, scanning magnetic induction tomography," *Proc. SPIE*, vol. 10132, Jun. 2017, Art. no. 10132172.

[14] J. R. Feldkamp and S. Quirk, "Optically tracked, single-coil, scanning magnetic induction tomography," *J. Med. Imag.*, vol. 4, no. 2, Jun. 2017, Art. no. 023504.

[15] J. R. Feldkamp and S. Quirk, "Internal magnetic induction tomography using a single coil," *Prog. Electromagn. Res.*, vol. 164, pp. 97–107, Jan. 2019.

[16] F. A. C. Viana, G. Venter, and V. Balabanov, "An algorithm for fast optimal latin hypercube design of experiments," *Int. J. Numer. Methods Eng.*, vol. 82, no. 2, pp. 135–156, Apr. 2010.

[17] J. R. Feldkamp and S. Quirk, "Coil geometry effects on scanning single-coil magnetic induction tomography," *Phys. Med. Biol.*, vol. 62, no. 17, pp. 7097–7113, Aug. 2017.

[18] H. Kaur and R. Ni, "ECG signal denoising with Savitzky-Golay filter and discrete wavelet transform (DWT)," *Int. J. Eng. Trends Technol.*, vol. 36, no. 5, pp. 266–269, Jun. 2016.

[19] *LDC1101 1.8-V High-Resolution, High-Speed Inductance-to-Digital Converter*, Texas Instrum., Dallas, TX, USA, Oct. 2016.

[20] G. J. Palacky, "Resistivity characteristics of geologic targets," in *Electromagnetic Methods in Applied Geophysics*, vol. 1, M. N. Nabighian, Ed. Society of Exploration Geophysicists, 1987, ch. 3, pp. 53–129. [Online]. Available: https://pubs.geoscienceworld.org/books/book/2079/Electromagnetic-Methods-in-Applied-Geophysics

[21] J. R. Feldkamp, "Inversion of an inductive loss convolution integral for conductivity imaging," *Prog. Electromagn. Res. B*, vol. 74, pp. 93–107, Jan. 2017.

[22] J. R. Feldkamp and S. Quirk, "Validation of a convolution integral for conductivity imaging," *Prog. Electromagn. Res. Lett.*, vol. 67, pp. 1–6, Jan. 2017.

[23] I. S. Gradshteyn and I. M. Ryzhik, *Table of Integrals, Series and Products, Corrected and Enlarged Edition*, A. Jeffrey, Ed. New York, NY, USA: Academic, 1980.

[24] L. Lapidus and G. F. Pinder, *Numerical Solution of Partial Differential Equations in Science and Engineering*. Hoboken, NJ, USA: Wiley, 1982.

[25] M. Kang and B. Vidakovic, "WavmatND: A MATLAB package for non-decimated wavelet transform and its applications," Apr. 2016, *arXiv:1604.07098*. [Online]. Available: http://arxiv.org/abs/1604.07098

[26] L. Eldén, "Algorithms for the regularization of ill-conditioned least squares problems," *BIT*, vol. 17, no. 2, pp. 134–145, Jun. 1977.

[27] M. Donatelli, A. Neuman, and L. Reichel, "Square regularization matrices for large linear discrete ill-posed problems," *Numer. Linear Algebra Appl.*, vol. 19, no. 6, pp. 896–913, Dec. 2012.

[28] M. A. Kandadai, J. L. Raymond, and G. J. Shaw, "Comparison of electrical conductivities of various brain phantom gels: Developing a 'brain gel model'," *Mater. Sci. Eng., C*, vol. 32, no. 8, pp. 2664–2667, Dec. 2012.

[29] A. D. Wiles, D. G. Thompson, and D. D. Frantz, "Accuracy assessment and interpretation for optical tracking systems," *Proc. SPIE*, vol. 5367, pp. 421–432, May 2004.